New geological insights into the Carmacks Copper Cu-Au-Ag deposit, central Yukon (Yukon MINFILE 115I008)

N. Kovacs*, M.M. Allan
Mineral Deposit Research Unit, University of British Columbia

A. Zagorevski
Geological Survey of Canada

J.E. Milton
Copper North Mining Corporation

C.J.R. Hart
Mineral Deposit Research Unit, University of British Columbia

Kovacs, N., Allan, M.M., Zagorevski, A., Milton, J.E. and Hart, C.J.R., 2017. New geological insights into the Carmacks Copper Cu-Au-Ag deposit, central Yukon (Yukon MINFILE 115I008). *In:* Yukon Exploration and Geology 2016, K.E. MacFarlane and L.H. Weston (eds.), Yukon Geological Survey, p. 117-140.

ABSTRACT

The Carmacks Copper Cu-Au-Ag deposit is hosted in compositionally heterogeneous, foliated and folded, and variably migmatitic metamorphic rocks, which occur as elongate, NNW-trending inliers in Early Jurassic granitoid rocks of the Granite Mountain batholith. Hypogene copper mineralization is restricted to metamorphic host rocks, and occurs both as foliation-parallel chalcopyrite-dominant stringers in schistose rocks, and as net-textured bornite-chalcopyrite-dominant sulphides in the migmatitic rocks prevalent along the eastern margin of the largest metamorphic inlier. The latter style of mineralization is interpreted to originate from a sulphide melt phase generated during partial melting of a previously mineralized protolith, during emplacement of the Granite Mountain batholith.

* *nkovacs@eoas.ubc.ca*

INTRODUCTION

The Carmacks Copper belt is a northwest trending corridor of mineralization that includes the Carmacks Copper Cu-Au-Ag (Yukon MINFILE 115I008) and Minto Cu-Au (Yukon MINFILE 115I021 and 115I022) deposits, as well the Stu Cu-Ag prospect (Yukon MINFILE 115I011) in west-central Yukon (Fig. 1). These occurrences are distinctive in that they are metamorphosed and exhibit ductile deformation, and as a result, interpretations of ore genesis have been controversial. Previous workers have classified the mineralization as metamorphosed volcanogenic massive sulphide (Pearson, 1977; Pearson and Clark, 1979), metamorphosed red-bed copper (Sinclair, 1977), and deformed copper-gold porphyry (Tafti, 2005). Another interpretation of the Minto deposit is genesis in a shear-hosted magmatic-hydrothermal system, in which mineralization formed in the mid-crustal roots of a porphyry system (Hood *et al.*, 2008). Exploration for additional mineralized zones and for similar copper-gold mineralization in the region has in part been hindered by the lack of a structural or genetic model for the deposits.

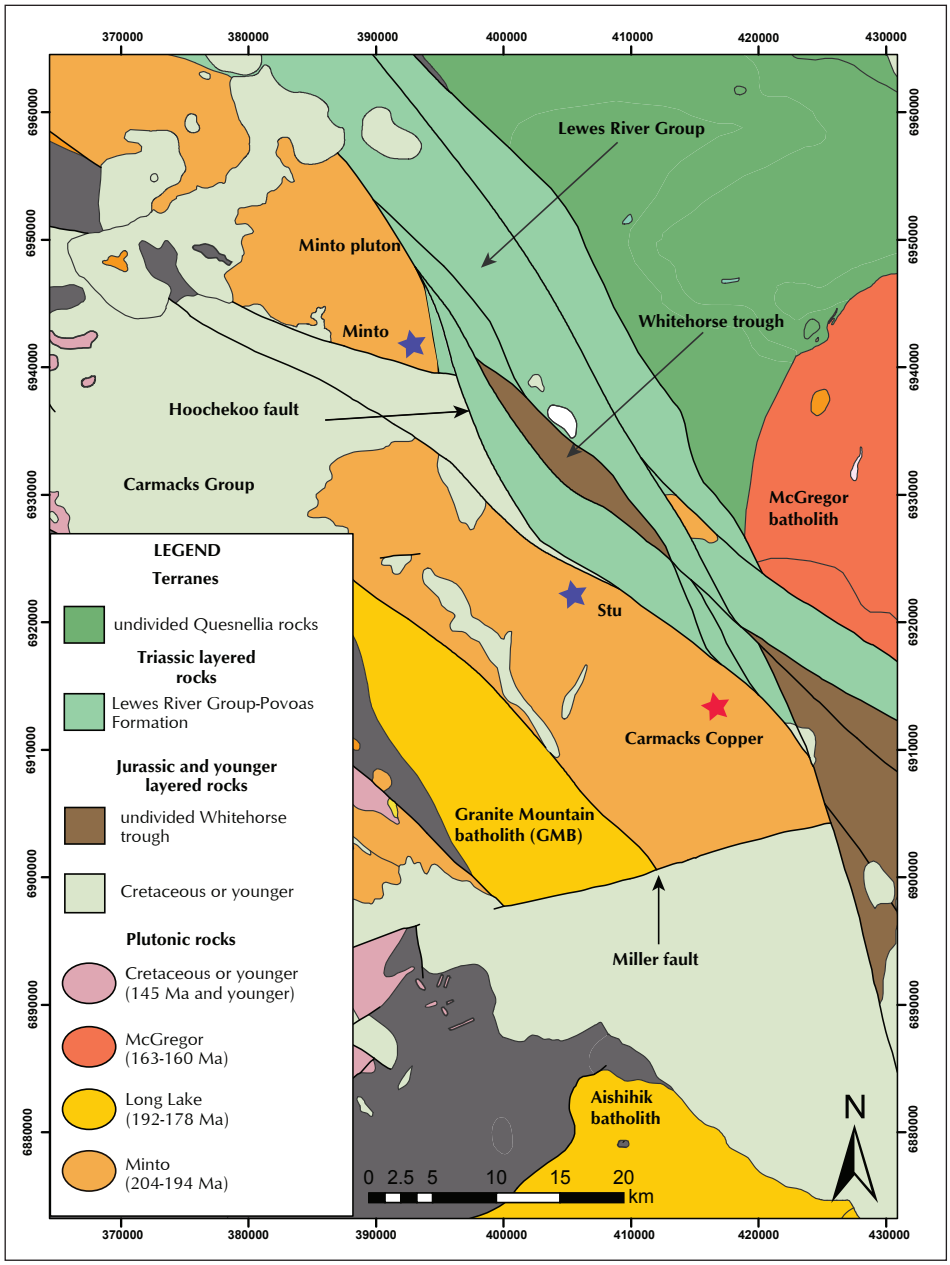

Figure 1. *Simplified regional geological map showing the location of the Carmacks Copper and Minto deposits. Geological information from Yukon Geological Survey (2015).*

The Carmacks Copper deposit, formerly known as the Williams Creek deposit, contains a measured and indicated resource of 15.69 million tonnes of oxide mineralization grading 0.94% copper, 0.38 g/t gold, and 3.97 g/t silver and 8.07 million tonnes of sulphide material (0.68% copper, 0.18 g/t gold, and 2.3 g/t silver) below the oxide (Copper North Mining Corp., 2016). An additional inferred resource comprises 0.91 million tonnes of oxide material grading 0.45% copper, 0.12 g/t gold, and 1.9 g/t silver and 8.41 million tonnes of sulphide mineralization grading 0.63% copper, 0.15 g/t gold, and 2.0 g/t silver. In this contribution, we describe metamorphic host rocks and plutonic phases of the Granite Mountain batholith (GMB) at the Carmacks Copper deposit, and provide a chronological framework for the various magmatic, structural, metamorphic and mineralizing events. This field-based geologic study of the Carmacks Copper deposit has broader implications for the metallogeny of the Carmacks Copper belt, and for mineral prospectivity associated with Late Triassic to Jurassic plutonic rocks in Yukon.

HISTORY

The first copper-gold mineralization in the Carmacks area was found by G.M. Dawson in 1887 at the Hoocheekoo bluffs along the Yukon River (Yukon MINFILE 115I013). The subsequent discovery of the Casino Cu-Au-Mo porphyry deposit spurred exploration in the Carmacks area, leading to the discovery of surface mineralization at the Carmacks Copper deposit in 1970 by J. Grant Abbott during reconnaissance prospecting and geochemical sampling (Abbott, 1971). The deposit has been the subject of intermittent exploration since the 1970s. Exploration was renewed in 2014 and a new development plan was proposed; oxide ore would be extracted in an open-pit operation, followed by agitated tank leaching, recovery of cathode copper through Solvent Extraction Electrowinning (SX-EW), and recovery of gold and silver in a cyanide circuit by carbon-in-leach (CIL; Copper North Mining Corp., 2016).

Zones 1, 4 and 7 of the deposit comprise the majority of the economic mineralization (Fig. 2), and zones 2000S, 12 and 13 were added to the resource in 2015.

PREVIOUS WORK

Initial interpretations were that copper mineralization at Carmacks Copper was contained within elongate roof pendants of quartz-biotite/hornblende-feldspar gneiss and feldspar porphyritic diorite enclosed within unmineralized granodiorite (Abbott, 1971). Although analogies were made to the porphyry copper model, it was noted that the lack of intense hydrothermal alteration could suggest an alternative model (Abbott, 1971). Sinclair (1977) proposed that the mineralized zones at both Minto and Carmacks Copper deposits represent poorly digested, migmatitic sedimentary or volcanic rocks. Pearson and Clark (1979) interpreted the Minto deposit as a deformed, hydrothermal deposit. Tafti and Mortensen (2004) provided the first geochronological constraints and geochemical characterization of the Carmacks Copper (Williams Creek) and Minto deposits, and concluded that mineralization, deformation, magmatism, and exhumation took place within a narrow time interval in the Early Jurassic (Tafti, 2005). More recently, regional geochronological, lithogeochemical, and thermobarometric investigations of Late Triassic to Early Jurassic magmatism in Yukon provided new opportunities to assess the tectono-magmatic context of Carmacks Copper and other ore deposits in this time interval (Colpron *et al.*, 2016a; Joyce *et al.*, 2016; Topham *et al.*, 2016; Allan *et al.*, 2013).

REGIONAL SETTING

Calc-alkaline to alkaline magmatism associated with the Mesozoic Quesnellia and Stikinia terranes is responsible for the proliferation of Late Triassic to Early Jurassic porphyry Cu (Au-Mo) deposits in British Columbia (Nelson *et al.*, 2013). In Yukon, dominantly plutonic equivalents of these Middle Triassic to Early Jurassic igneous rocks have recently been subdivided into five distinct suites. From oldest to youngest, these include the Stikine suite (*ca.* 216-206 Ma), Minto suite (*ca.* 204-194 Ma), Long Lake suite (*ca.* 192-178 Ma), Bryde suite (*ca.* 172-168 Ma) and McGregor suite (163-160; Colpron *et al.*, 2015, 2016b; Sack *et al.*, 2015) (Fig. 1).

The Early Jurassic Granite Mountain batholith (GMB) intrudes mid-Paleozoic metamorphic rocks of the Yukon-Tanana terrane to the southwest, and is in fault contact with the Povoas Formation of the Upper Triassic Lewes River Group of Stikinia to the northeast (Tempelman-Kluit, 1984; Fig. 1). The GMB hosts Cu-Au-Ag mineralization at the Carmacks Copper deposit (Yukon MINFILE 115I008), Minto (Yukon MINFILE 115I021 and 115I022) mine, and Stu prospect (Yukon MINFILE 115I011).

The eastern flank of the GMB comprises rocks of the Minto suite, whereas the western flank is composed of distinctly younger rocks of the Long Lake suite. Regionally, the Long Lake suite ranges from quartz monzonite to tonalite in composition and consists of three different phases: medium-grained, equigranular granodiorite, porphyritic granodiorite, and porphyritic granite to quartz monzonite phase (Joyce *et al.*, 2016). The Minto suite ranges from quartz monzodiorite to tonalite (Joyce *et al.*, 2016) and is currently the only known Late Triassic to Early Jurassic suite to host copper mineralization in Yukon (Sack *et al.*, 2015). The contact between the Minto and Long Lake phases of the GMB is mapped 10 km west of the Carmacks Copper deposit (Colpron *et al.*, 2015b; Fig. 1), and coincides with a major magnetic lineament (Sánchez *et al.*, 2013). The GMB is unconformably overlain by mafic to intermediate volcanic rocks of the Late Cretaceous Carmacks Group – a thick, sheet-like succession that covered much of Yukon south of the Tintina fault (Tempelman-Kluit, 1984; Fig. 1). Locally, dacite dikes inferred to be coeval with Late Cretaceous volcanism cut the GMB (Tempelman-Kluit, 1984).

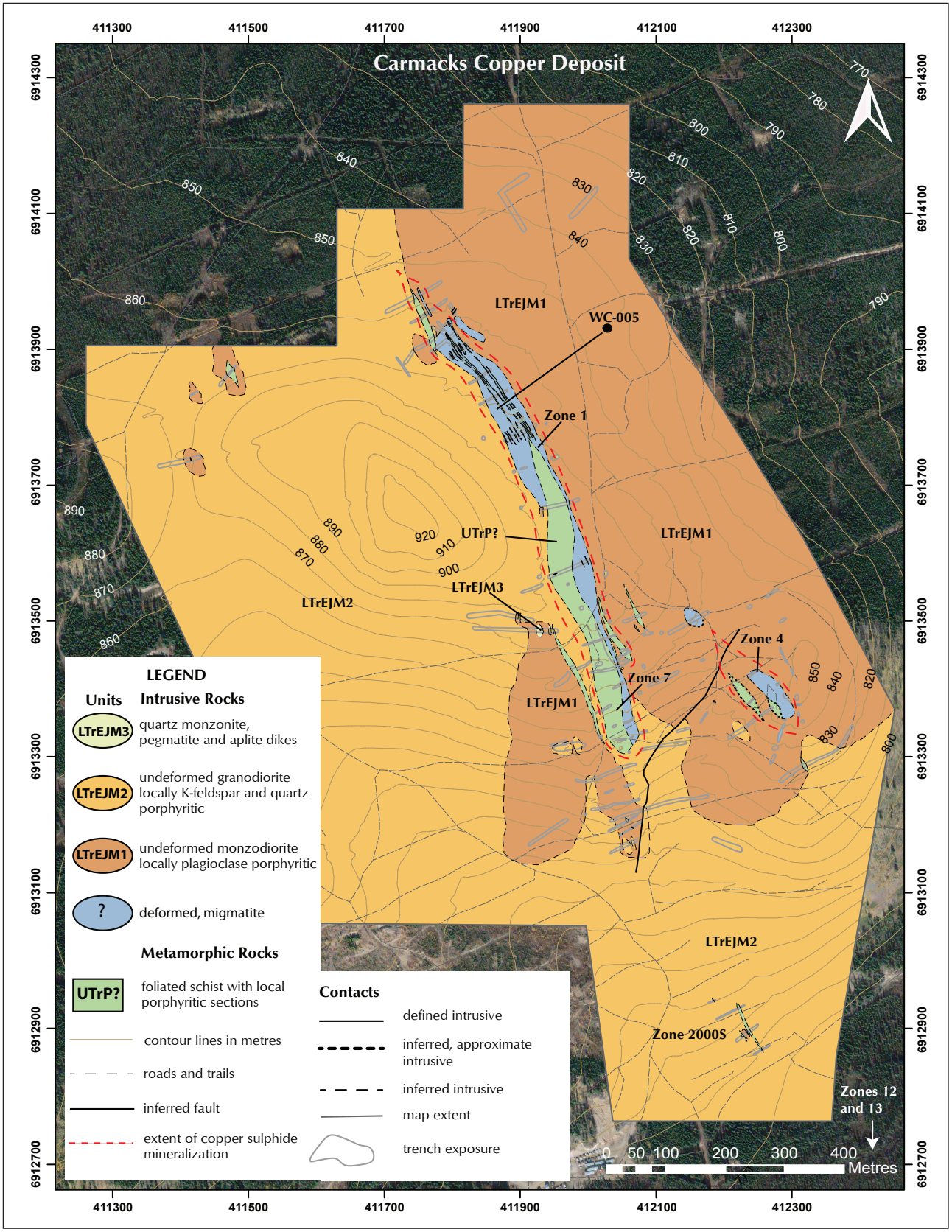

Figure 2. *Geological map of the Carmacks Copper deposit area based on 2015 and 2016 field work.*

DEPOSIT GEOLOGY

The geology of the Carmacks Copper deposit area is characterized by intermediate plutonic rocks of the GMB containing NNW-trending inliers of compositionally heterogeneous, foliated and folded, and variably migmatitic metamorphic rocks (Fig. 2). The metamorphic rocks are affected by an early, foliation (S_1), which is dominantly NNW-striking and steeply dipping. The largest metamorphic inlier, comprising zones 1 and 7 of the Carmacks Copper deposit (Fig. 2), is intruded by two compositionally distinct, undeformed, plutonic phases (I_1 and I_2; LTrEJM1 and LTrEJM2 in Fig. 2, respectively). Metamorphic rocks are also intruded by quartz monzonite, aplite, and pegmatite dikes (I_3; LTrEJM3), which also cross-cut the I_1 and I_2 intrusive phases. Migmatitic rocks interpreted to have formed from the partial melting of metamorphic rocks during the emplacement of I_1 (and I_2?), are preferentially developed along the eastern margin of the main metamorphic inlier, which also coincides with the bulk of mineralization at the Carmacks Copper deposit (Fig. 2). A second phase of ductile deformation (D_2) is responsible for the local development of crenulation cleavage (S_2) in the metamorphic rocks, and is correlated with mesoscopic folding of metamorphic rocks and I_3 dikes, in which dikes are locally dismembered as boudins along fold limbs or as rootless fold hinges. Preliminary high-precision U-Pb zircon ages of the I_3 dikes suggests they are younger than the massive I_1 and I_2 phases of the GMB (R. Friedman, pers. comm., 2016), which requires that D_2 deformation post-dates emplacement of the GMB.

METAMORPHIC ROCKS

Metamorphic rocks occur as inliers within massive plutonic rocks of the GMB. The largest of these inliers is an elongate NNW-trending, 3 km-long and 20 to 100 m-wide body that hosts the bulk of the deposit's resource in zones 1 and 7 (Fig. 2). The metamorphic sequence comprises dark-grey, fine-grained, and strongly foliated feldspar-amphibole schist and quartz-plagioclase-biotite schist that are interlayered on the scale of 0.5 to 1 m. The quartz-plagioclase-biotite schist is distinctively brown-weathered (Fig. 3a).

The feldspar-amphibole schist generally contains approximately 60-65% plagioclase, 25-30% hornblende and minor quartz (1%) with locally developed biotite (10-12%; Fig. 3b). Feldspar grains are anhedral to subhedral with undulose extinction, consertal grain boundaries, and are often rimmed by sub-grains. Hornblende is medium-grained and subhedral. Accessory minerals include titanite and epidote. Foliation (S_1) is defined by the alignment of hornblende grains, which commonly form 1-2 cm-wide mafic domains. Hornblende is commonly altered to chlorite and/or biotite. Plagioclase grains are variably altered to K-feldspar and sericite.

The quartz-plagioclase-biotite schist typically contains 70% plagioclase, 20% biotite and 10% quartz (Fig. 3c). Both plagioclase and quartz form anhedral, equant grains, but quartz is finer grained (0.2-0.4 mm) and occurs interstitially to plagioclase grains (0.5-0.6 mm). Biotite is interstitial to plagioclase and quartz and forms subhedral, acicular grains.

The foliation (S_1) is defined by alignment of biotite in the quartz-plagioclase-biotite schist. This foliation is locally overprinted by a granoblastic texture, especially near the contact with the felsic intrusive rocks of the GMB. Plagioclase is slightly sericite-altered.

Locally, massive, clinopyroxene-phyric metagabbro is in texturally gradational contact with feldspar-amphibole schist. These rocks contain stubby, coarse-grained, glomeroporphyritic hornblende in a medium-grained groundmass of 60% plagioclase, 15-20% hornblende and minor epidote and biotite (Fig. 3d). The hornblende glomerocrysts commonly pseudomorph clinopyroxene, suggesting a metamorphic origin for hornblende and clinopyroxene as a phenocryst phase in the protolith. Medium-grained hornblende in the groundmass occurs interstitially to plagioclase. A few of these grains exhibit secondary deformation twinning and are slightly kinked. Plagioclase is medium grained with subhedral to anhedral habit. Epidote is fine grained, acicular and locally intergrown with hornblende. In a few samples, epidote exhibits an embayed, skeletal texture. A few poikilitic epidote grains contain plagioclase and opaque inclusions. Biotite replacement of hornblende is common. Plagioclase is moderately sericite-altered. In a few places, biotite is altered to chlorite. This unit is locally cut by K-feldspar veins and a later stage of epidote veinlets.

Figure 3. *Metamorphic rocks of the Carmacks Copper deposit:* ***(a)*** *outcrop of interlayered quartz-plagioclase-biotite schist (left) and feldspar-amphibole schist (right);* ***(b)*** *cross-polarized microphotograph of feldspar-amphibole schist;* ***(c)*** *cross-polarized microphotograph of quartz-plagioclase-biotite schist; and* ***(d)*** *microphotograph of hornblende-glomeroporphyritic metagabbro (plane-polarized light). The hornblende aggregates are interpreted as pseudomorphs after clinopyroxene. pl=plagioclase; hbl=hornblende.*

Migmatites

Migmatitic rocks host hypogene mineralization in zones 1, 4 and 7 of the deposit (Fig. 2), and are preferentially developed along the eastern flank of the main metamorphic inlier. Migmatite comprises four texturally and mineralogically distinctive phases. (1) Lighter-coloured, coarse-grained sections dominantly consisting of feldspar and quartz define the leucosome (Fig. 4a). (2) Black, mafic phases consisting mainly of hornblende and biotite are the melanosome (Fig. 4b). (3) Domains within the migmatite unit that are apparently unaffected by partial melting define the paleosome, and consist of quartz-plagioclase-biotite schist with slightly coarsened grains and pseudo-granoblastic texture. (4) White, medium-grained, folded, foliation-parallel (S_1), leucocratic veins are common within the quartz-plagioclase-biotite schist (Fig. 4c).

Leucosome typically contains 40% plagioclase, 25-30% K-feldspar, 10-15% hornblende and less than 5% quartz

and biotite (Fig. 4a). Plagioclase and K-feldspar form anhedral, medium to coarse grains. Hornblende is coarse grained, subhedral and typically poikilitic with respect to inclusions of plagioclase, epidote, quartz and copper sulphides. In a few places, hornblende grains are fractured and exhibit secondary deformation twinning. Quartz forms anhedral, equant, and fine grains that are interstitial to plagioclase and K-feldspar. Biotite is fine grained and interstitial to feldspar. Locally, epidote occurs with an unusual growth habit in the form of narrow (0.05 mm) rims on plagioclase in contact with copper sulphides. Titanite is the main accessory mineral and occurs as anhedral, fine-grained, isolated patches. Net-textured copper sulphides occupy the groundmass interstitial to plagioclase and hornblende. Plagioclase and K-feldspar are slightly sericite-altered; hornblende and biotite are both moderately chlorite-altered.

Melanosome typically contains 70-80% hornblende and 15-20% biotite (Fig. 4b). Hornblende forms stubby, anhedral, medium-sized grains. Biotite is anhedral and medium grained. Local, foliated domains of the melanosome contain folded, coarse-grained biotite. Both biotite and hornblende grains are commonly altered to chlorite.

Leucocratic veins typically have sharp contacts and occur as blebs or narrow (1-3 cm-wide), rootless, ptygmatic folds within the quartz-plagioclase-biotite schist. These veins consist of anhedral, medium-grained (0.5-0.8 mm) quartz (80%) and plagioclase (20%). The veins are rimmed by a thin (1-3 mm-wide), biotite-rich selvedge (Fig. 4c). Locally these veins contain net-textured copper sulphides.

PLUTONIC ROCKS

Two compositionally distinct phases of the GMB are present on either side of the main metamorphic inlier at the Carmacks Copper deposit (zones 1 and 7; Fig. 2). The deposit is flanked to the east by a medium-grained monzodiorite (I_1; LTrEJM1), and to the west by a coarse to medium grained, K-feldspar ± quartz-phyric granodiorite (I_2; LTrEJM2; Fig. 2).

The eastern phase (I_1) is characterized by monzodiorite with minor diorite and monzonite. These rocks are generally white, medium grained and unfoliated. The rocks contain 40-60% plagioclase, 25-30% hornblende, 15-25% K-feldspar, 5-7% biotite and less than 5% quartz (Fig. 5a). Biotite is commonly absent. Both K-feldspar and plagioclase occur as medium (1-2 mm), anhedral grains with consertal grain boundaries. A plagioclase porphyritic phase (1-2 cm) is commonly gradational to the non-porphyritic phase. Fine-grained, anhedral quartz is interstitial relative to plagioclase and K-feldspar. Apatite and titanite are the main accessory minerals. Hornblende is anhedral, commonly embayed or skeletal, and slightly altered to chlorite, epidote and biotite.

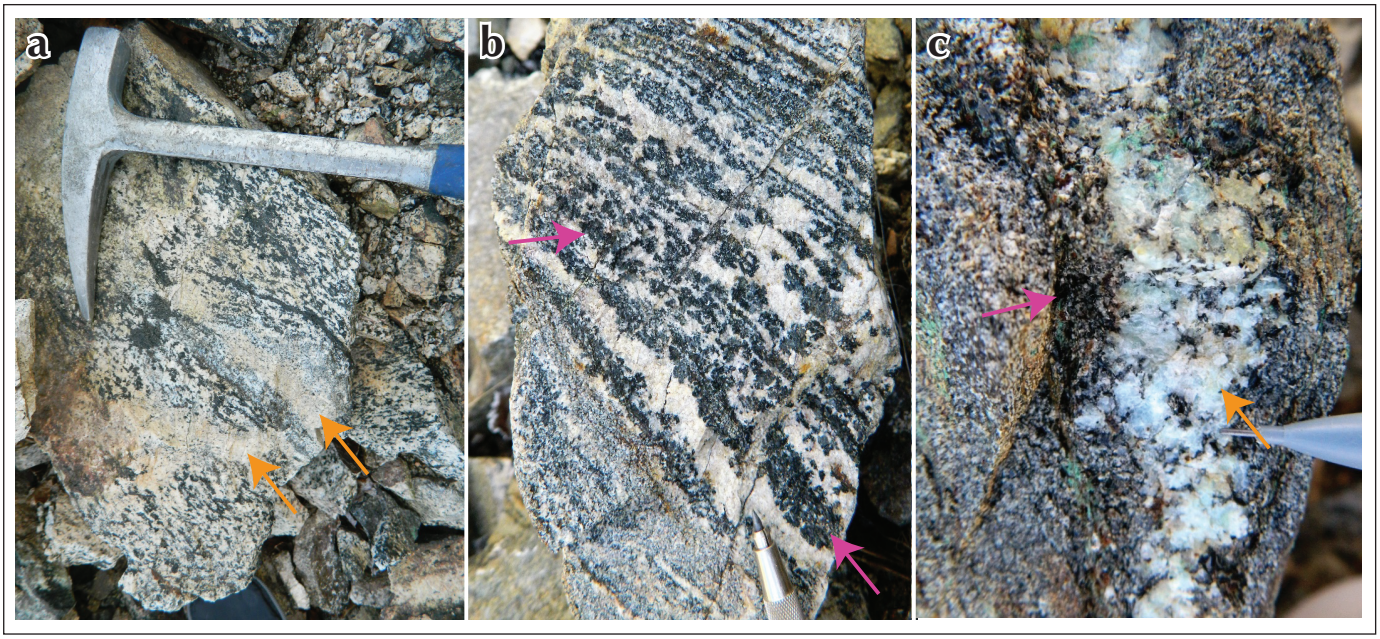

Figure 4. *Migmatitic rocks of the Carmacks Copper deposit.* ***(a)*** *Heterogeneous migmatitic textures. Orange arrows indicate leucosome;* ***(b)*** *detail showing coarse-grained amphibole-dominant melanosome (black) indicated by the magenta arrows; and* ***(c)*** *detail showing a leucocratic veinlet with blue-green copper oxides after copper sulphides. Orange arrows indicate the leucosome bordered by mafic selvedge (magenta arrow).*

The western phase (I_2) is dominated by quartz diorite to granodiorite, with minor monzogranite and quartz monzodiorite. The granodiorite and quartz-diorite members are both medium to coarse grained, and are in gradational contact with each other. The granodiorite is K-feldspar-quartz porphyritic (Fig. 5b), whereas the quartz diorite only contains quartz phenocrysts (Fig. 5c). K-feldspar phenocrysts range in length from 10-20 mm, and are generally randomly oriented, although a weak magmatic foliation is locally present. The I_2-phase rocks typically contain 40% plagioclase, 25% K-feldspar, 10-12% biotite and 4-5% hornblende. Quartz is abundant (25-45%) and occurs both as anhedral, coarse grains (1-2 mm) and as interstitial, fine grains (0.5-0.7 mm). Myrmekitic intergrowths of quartz and feldspar are extensively developed along quartz-plagioclase grain boundaries. The mafic phase includes both biotite and hornblende that are generally anhedral to subhedral. Hornblende is poikilitic, with inclusions of quartz and epidote. Some of the larger grains also exhibit deformation twinning and undulose extinction. Anhedral, lenticular epidote, and titanite are the main accessory minerals. Plagioclase is moderately sericite-altered and locally, intensely K-feldspar-altered. Both biotite and hornblende are slightly altered to chlorite.

The I_3 intrusive phase (LTrEJM3) includes folded and locally boudinaged dikes of quartz monzonite, granite pegmatite and aplite that cross-cut all units described above, and thus they represent the youngest unit in the deposit.

The quartz monzonite consists of plagioclase (40-50%), K-feldspar (25-40%), quartz (10-25%) and biotite (5-12%). Plagioclase and K-feldspar form subhedral, coarse grains (2.5-4 mm). Half-corona textures of K-feldspar on plagioclase locally occurs. Microperthitic intergrowth is common and it is mainly exposed on the albite twinned plagioclase grains. Quartz is fine grained (0.5-1 mm), anhedral, and forms consertal grain boundaries that occupy the interstitial spaces between plagioclase and K-feldspar. In a few places, micrographic intergrowth of plagioclase and quartz occurs near the grain boundaries. Biotite is subhedral, medium grained (0.5-1 mm), and occurs interstitially to feldspar grains, locally forming glomeroporphyritic clusters; both are slightly sericite-altered.

Granitic pegmatite is white and massive textured. The modal mineralogy consists of 50-60% plagioclase, 30-40% K-feldspar and 10-12% biotite. The aplite dikes are white, fine grained and sugary textured. The modal mineralogy of aplite is 40% plagioclase, 30% K-feldspar and 30% quartz. The I_3 intrusions are typically unaltered.

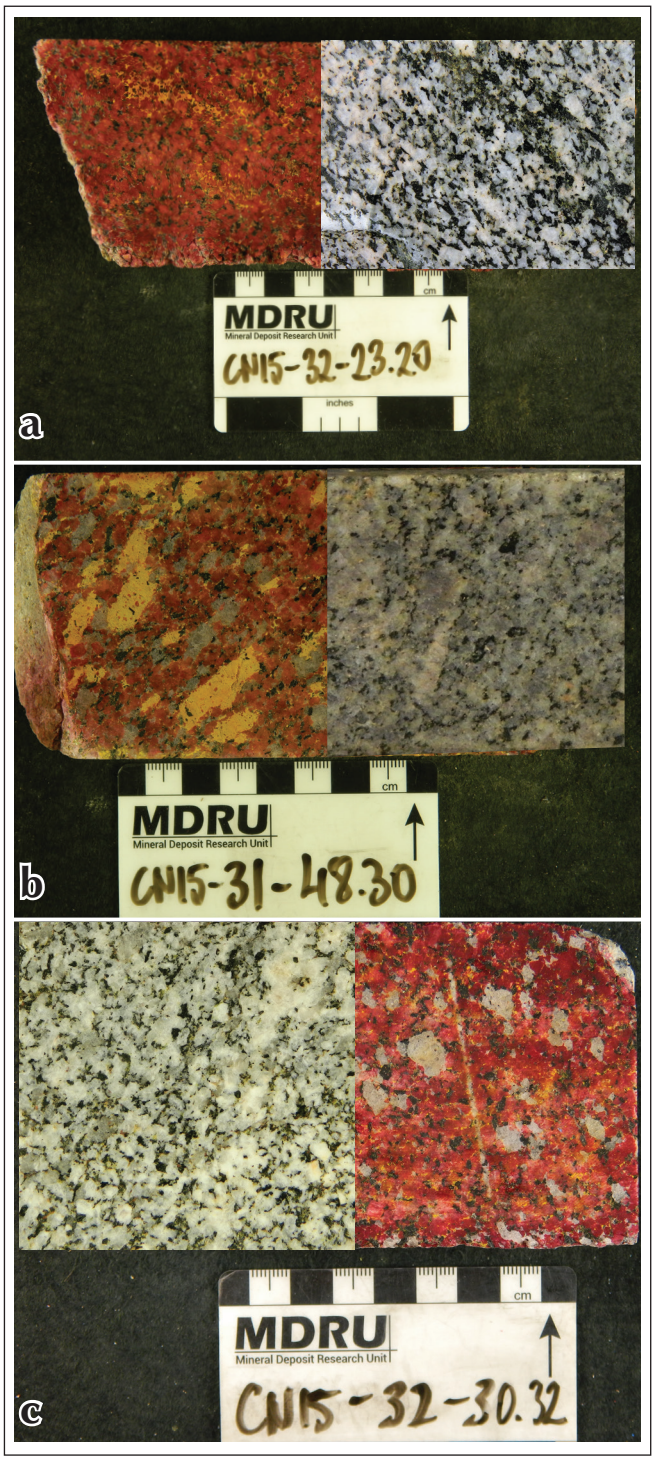

Figure 5. *Plutonic rocks of the Granite Mountain batholith in the vicinity of the Carmacks Copper deposit.* ***(a)*** *Monzodiorite of the eastern plutonic phase (I_1; stained slab on left);* ***(b)*** *K-feldspar megacrystic granodiorite of the western phase (I_2; stained slab on left); and* ***(c)*** *quartz diorite of the western phase (I_2; stained slab on right). Red colours on stained slabs correspond to plagioclase, whereas yellow colours correspond to K-feldspar. Unstained, milky white grains are quartz.*

Modal mineralogy and geochemistry

Modal proportions of quartz, K-feldspar and plagioclase in fresh plutonic rocks were determined from digital scans of cobaltinitrite and amaranth red stained drill core slabs with ImageJ software (plagioclase stained red; K-feldspar stained yellow). Plutonic rock classifications based on these proportions were made using the quartz-alkali feldspar-plagioclase (QAP) scheme of Le Bas and Streckeisen (1991). Plutonic rocks are divided into two compositionally distinct groups based on this classification. Rocks sampled from the western I_2 phase are distinctly quartz-rich relative to quartz-poor rocks of the eastern I_1 phase (Fig. 6).

Major, trace, and rare-earth element compositions were determined for 20 samples of mainly unmineralized and undeformed intrusive rocks collected from diamond drill holes and trenches (Fig.7; Appendix 1). Samples were fused with a lithium borate flux and a suite of 45 elements was analyzed by ICP-MS. Major element oxides were analyzed by x-ray fluorescence (XRF) spectrometry.

The eastern phase (I_1) is monzodioritic to monzonitic in composition based on total alkalis versus silica (Le Bas *et al.*, 1986; Fig. 7a), and is of alkaline (Irvine and Baragar, 1971; Fig. 7b) and metaluminous affinity (Frost and Frost, 2008; Fig. 7c). The tectonic discrimination diagrams of Whalen *et al.* (1987) and Pearce *et al.* (1984) classify these rocks as an I-type volcanic arc granitoid (Fig. 7d,e). The immobile element Zr/Ti vs. Nb/Y diagram of Pearce (1996) shows that intrusive rocks of the eastern phase compared to the western I_2 phase are less evolved, but have similar alkalinity (Fig. 7f).

Intrusive rocks of the western I_2 phase range from syenite, granodiorite, to granite in composition (Le Bas *et al.*, 1986; Fig. 7a). The total alkalis versus silica discrimination diagram of Irvine and Baragar (1971) classifies the western phase as subalkaline (Fig. 7b), and ranging from high-K to low-K series. All samples are metaluminous and weakly to moderately peraluminous (Fig. 7c) and are classified as volcanic arc (I-type) granitoid rocks (Pearce, 1984; Fig. 7d,e) with a slightly more fractionated geochemistry (Pearce, 1996; Fig. 7f). Granitic pegmatite plots closer to the alkaline apex of the AFM diagram (Irvine and Baragar, 1971), indicating that it likely represents late, evolved melt related to the western phase.

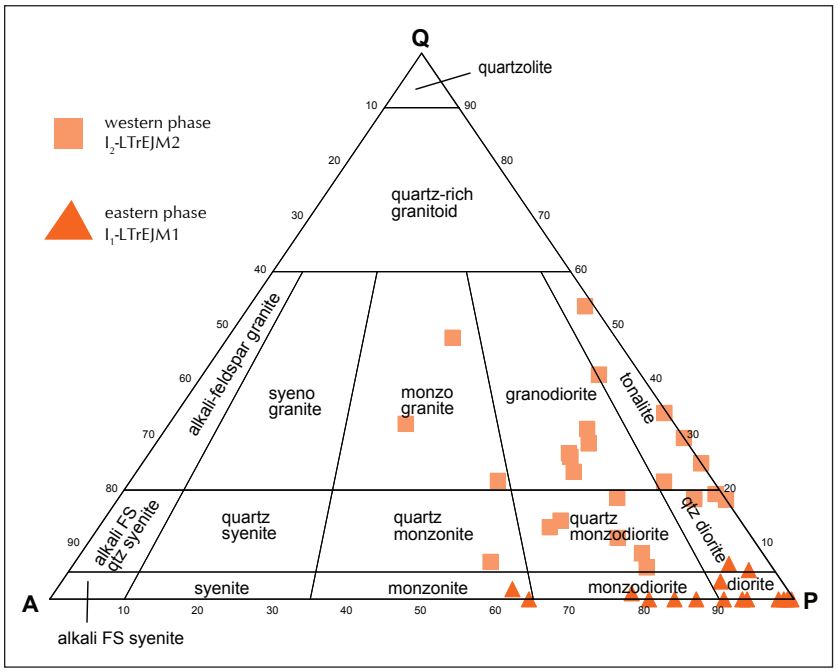

Figure 6. *Quartz-alkali feldspar-plagioclase (QAP) classification of plutonic rocks with <90% mafic mineral content (Le Bas and Streckeisen, 1991) using modal minerology determined from stained rock slabs.*

SUMMARY OF GEOLOGICAL EVENTS

Metamorphic rocks of the Carmacks Copper deposit preserve at least two phases of ductile deformation. A penetrative NNW-trending and steeply dipping (80-90°) foliation (S_1) represents an early phase of ductile deformation (D_1) that pre-dates the emplacement of the Granite Mountain batholith (Fig. 8a). This dominantly NNW-trending fabric mimics the orientation of the metamorphic inliers and the general map trend of mineralization (Fig. 2).

The eastern plutonic phase of the GMB (I_1) intrudes the metamorphic rocks and is likely responsible for partial melting of schistose rocks and formation of migmatite. A second phase of magmatism is characterized by the intrusion of the western plutonic phase (I_2). However, the preferential formation of migmatitic rocks along the I_1 intrusive contact suggests that the emplacement of I_2 did not lead to further migmatization of the metamorphic rocks. This suggests that only during emplacement of I_1 was the temperature of the metamorphic rocks sufficient to induce partial melting. Emplacement of either I_1 or I_2 could explain the local obliteration of planar fabrics through recrystallization (*i.e.*, grain size coarsening

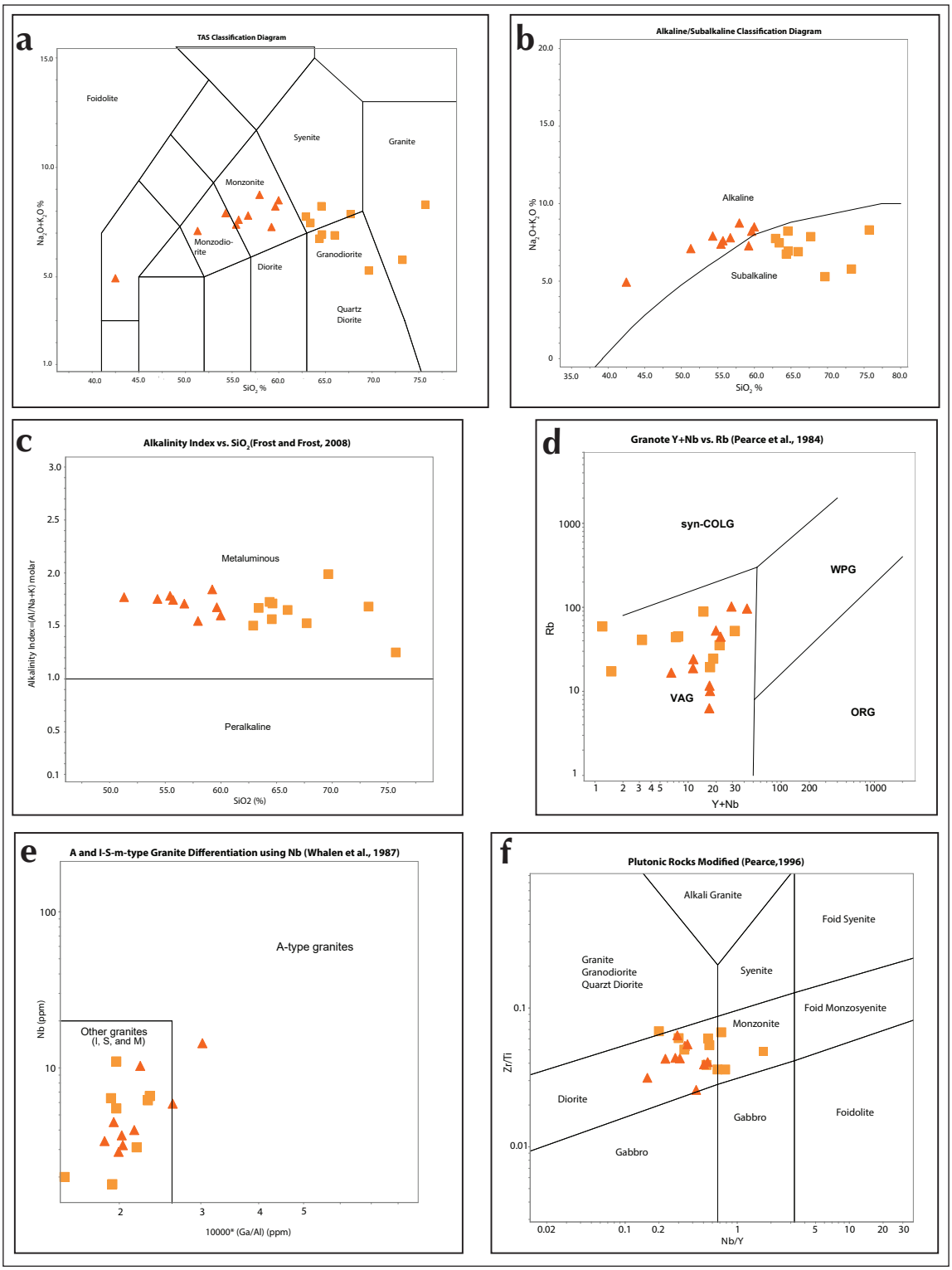

Figure 7. *Whole-rock geochemical plots.* ***(a)*** *Total alkali-silica (TAS) plot of representative intrusive phases (Le Bas et al., 1986);* ***(b)*** *total alkali versus silica diagram after Frost et al., (2001);* ***(c)*** *alkalinity index plot after Frost and Frost (2008);* ***(d)*** *tectonic discrimination diagram for collision zone intrusions after Harris et al. (1986);* ***(e)*** *A and I-S-M-type granite differentiation diagram after Whalen et al. (1987); and* ***(f)*** *immobile element Zr/Ti and Nb/Y diagram of Winchester and Floyd (1977), modified by Pearce (1996). Square symbols denoting the western phase are more fractionated than samples from the eastern phase (triangles).*

and formation of granoblastic textures). The third magmatic event (I_3) is marked by the intrusion of quartz monzodiorite, aplite and pegmatite dikes that crosscut all the other lithologies (Fig. 8b).

A second phase of ductile deformation (D_2) led to formation of locally developed crenulation in the metamorphic rocks (Fig. 8c), and is likely correlated with formation of tight to open folds of I_3 dikes and the metamorphic rocks they intrude (Figs. 8b and 9a). Progressive ENE-WSW directed shortening during D_2 deformation led locally to structural dismemberment of I_3 dikes into irregular, rootless bodies in fold hinges, and as boudinaged limbs (Figs. 8a and 9a). The axial planar fabric associated with these folds (S_2) is observed locally as high-angle relationships between metamorphic fabrics and rootless granitoid bodies in fold hinges (Fig. 9b). Migmatite and intrusive rocks of the I_2 western phase locally contain a tectonic foliation along their contact with the metamorphic rocks, which we tentatively correlate with S_2 fabrics formed within the metamorphic inlier. However, much of Granite Mountain batholith is unfoliated, presumably due to strain partitioning into rheologically weak schistose rocks. Dikes intruding these schistose rocks were affected by D_2, but boudinage of these bodies indicates that the temperature of deformation was below their solidus. A paragenetic summary of the geologic events described above is shown in Figure 10.

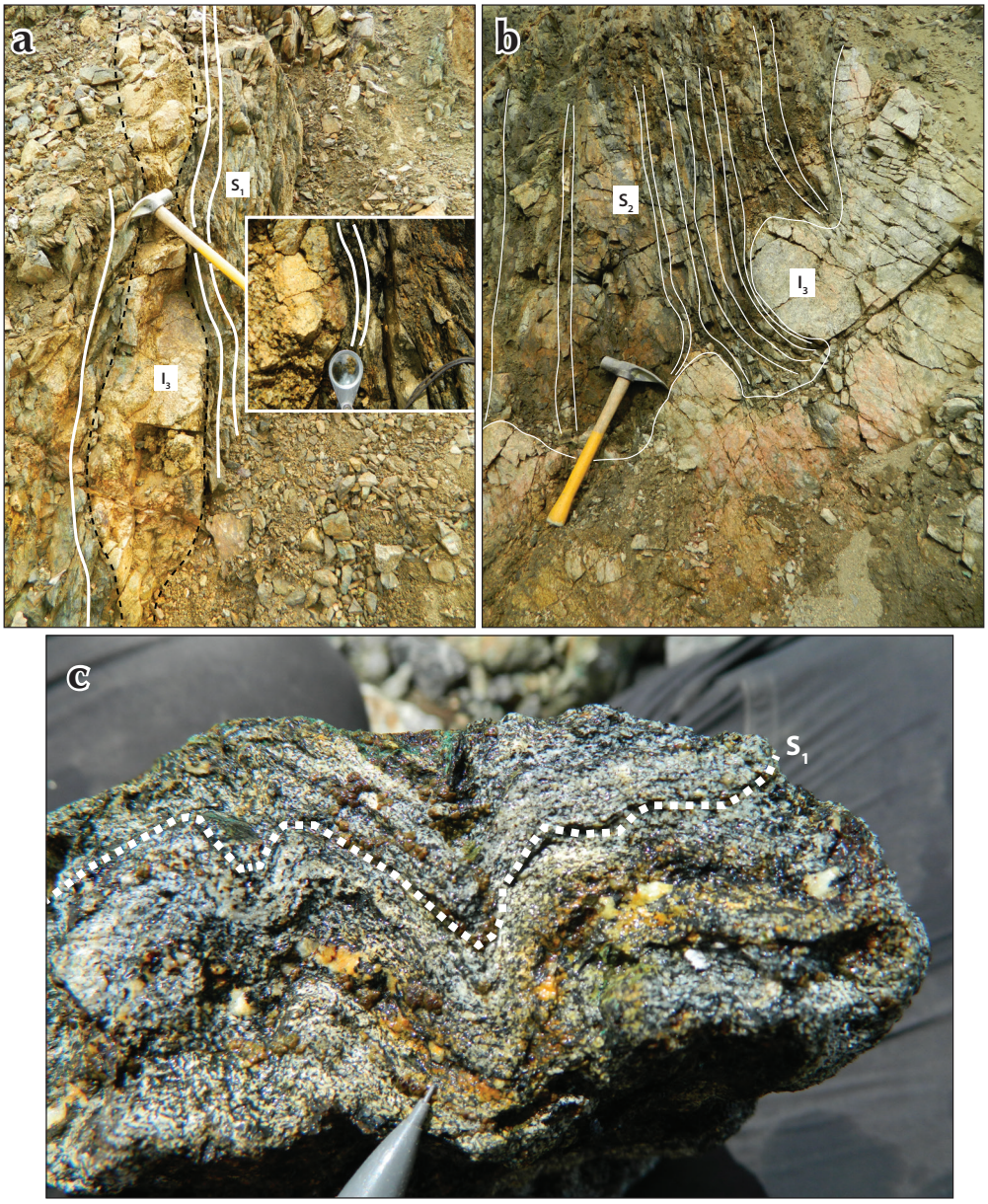

Figure 8. *Deformation features of the Carmacks Copper deposit.* ***(a)*** *Boudined quartz monzodiorite dike (I_3) in foliated feldspar-amphibole schist. I_3 dikes were affected by the latest D_2 deformation event;* ***(b)*** *dismembered I_3 dike in the hinge of a synform. Fabrics in the metamorphic rocks are interpreted as an axial planar cleavage (S_2) to the fold.* ***(c)*** *Crenulation in the quartz-plagioclase-biotite schist as a result of D_2 event.*

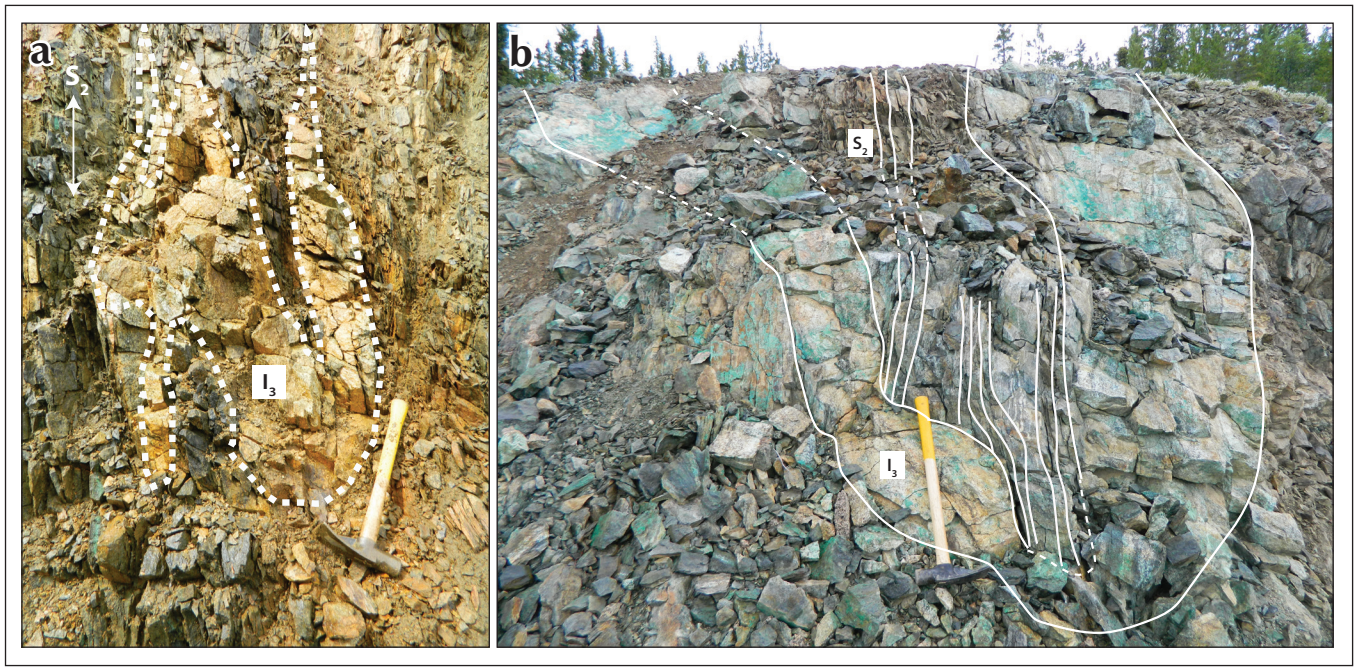

Figure 9. *Fold features of the Carmacks Copper deposit.* ***(a)*** *Folded I_3 dike. Note the axial planar cleavage (S_2) in the fold hinge; and* ***(b)*** *folded I_3 dike, looking north. Note the abundance of copper oxides.*

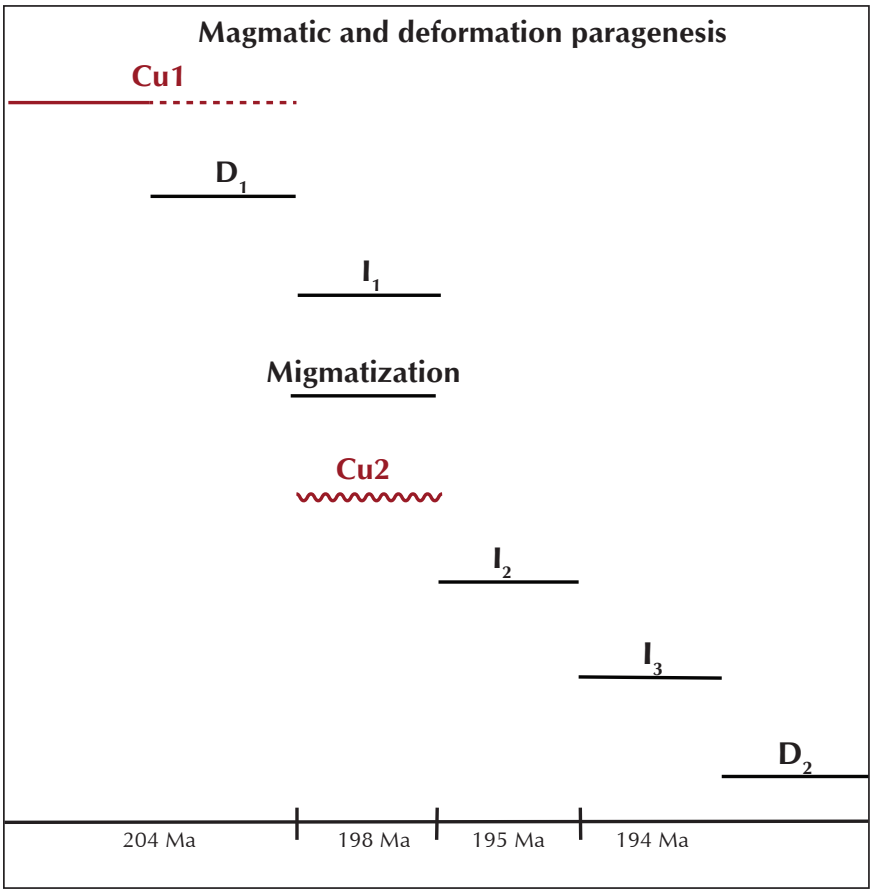

Figure 10. *Summary of magmatic (I), deformation events (D) relative to mineralization. Absolute ages are based on preliminary, unpublished U-Pb zircon and Re-Os results (R. Friedman, pers. comm., 2016; R. Creaser, pers. comm., 2016).*

Several late, E-W-trending brittle faults cut all previously described rock units and structural elements. These faults are observed in trenches and occur as prominent non-magnetic discontinuities in total magnetic field data. The faults are characterized by zones of hematite-carbonate-epidote-clay±chlorite alteration where they cut felsic plutonic rocks. Slicken-lines on hematitic or pyrolusite-coated fractures show subhorizontal plunge, indicating the latest movement on these faults is dominated by strike-slip motion. Fault breccia is rare and is not mineralized. The most significant brittle structure on the property is a NNE-trending, 1.5 km-long fault passing near the southern end of zone 7 and northern end of zone 4 (Fig. 2). This fault is post-mineralization and is potentially responsible for an apparent ~250 m of sinistral offset of metamorphic rocks and mineralization in zone 4 from zone 7. Regardless of its sense of displacement, this fault explains the southern termination of mineralization in zone 7 (Fig. 2). Although we infer that zone 4 could represent the offset continuation of zone 7, zone 4 may instead represent a separate inlier of mineralized metamorphic rock.

MINERALIZATION

Hypogene copper mineralization is mainly hosted by the feldspar-amphibole schist, quartz-plagioclase-biotite schist, and migmatitic rocks. Chalcopyrite and bornite are the main sulphide minerals, whereas pyrite is notably low. Locally, molybdenite is present in high concentrations in migmatite, but is sparse at the deposit scale. Magnetite is common in the western part of the deposit but minor elsewhere. Where hosted in schistose rocks, copper mineralization (Cu1) occurs as foliaform chalcopyrite-dominant stringers that parallel the dominant S_1 foliation (Fig. 11a). In contrast, mineralization hosted by migmatitic rocks occurs as net-textured intergrowths of bornite and chalcopyrite that occupy the interstices of generally fresh, magmatic silicate grains (Cu2; Fig. 11b). Foliaform Cu1 mineralization within the schists generally accounts for 1-2% of the rock volume. Chalcopyrite occurs as elongate, foliation-parallel blebs up to 1 mm with much less abundant bornite (Fig. 11c).

Net-textured copper sulphides form up to 20% of the rock by volume and include bornite (15%) and lesser chalcopyrite (4-5%). Bornite and chalcopyrite occur together in irregular net-textured domains up to 2-4 mm across that are clearly interstitial with respect to silicate grains. A few grains of bornite contain abundant exsolution blebs of chalcopyrite. Generally, chalcopyrite forms anhedral patches 1-1.8 mm across and is intimately intergrown with bornite. Both chalcopyrite and bornite are commonly replaced by digenite along 50 mm-wide fractures and grain margins. Hematite forms narrow (10 mm), irregular patches along fractures and the margins of bornite–chalcopyrite–digenite. Chalcocite (?) forms fine-grained, prismatic needles that occur at bornite-chalcopyrite grain boundaries.

Since the mineralization hosted by metamorphic rocks is S_1-parallel, it is concluded that copper mineralization was introduced to the protolith prior to D_1 deformation. Net-textured mineralization is restricted to migmatitic host rocks, which requires crystallization of igneous silicates from silicate melt, followed by precipitation of bornite and chalcopyrite from an immiscible sulphide liquid. We interpret that previously mineralized (Cu1) and deformed (D_1) rocks were heated to partial melting conditions in the thermal aureole of the GMB, in which copper and trace metals entered a mobile sulphide liquid phase that re-precipitated sulphides on cooling. Significantly, net-textured sulphides mantle unaltered plagioclase (60%) and hornblende (15%) in migmatitic rocks (Fig. 11d). The freshness of plagioclase and mafic mineral phases (excepting minor and late chlorite, sericite and carbonate alteration) suggests strongly that copper was not introduced at this stage by a hydrothermal fluid. If hydrothermal transport were the main mechanism of mineralization at the Cu2 stage, one would not only expect hydrolytic alteration of silicate phases, but replacement of Fe-bearing silicates by sulphide minerals.

The ore mineral distribution broadly tracks a western chalcopyrite zone that correlates to the metamorphic host rocks, and an eastern bornite-chalcopyrite-digenite zone that correlates with migmatitic host rocks (Fig. 2). A summary of mineralization related to deformation (Fig. 10) and lithology is demonstrated on Figure 12.

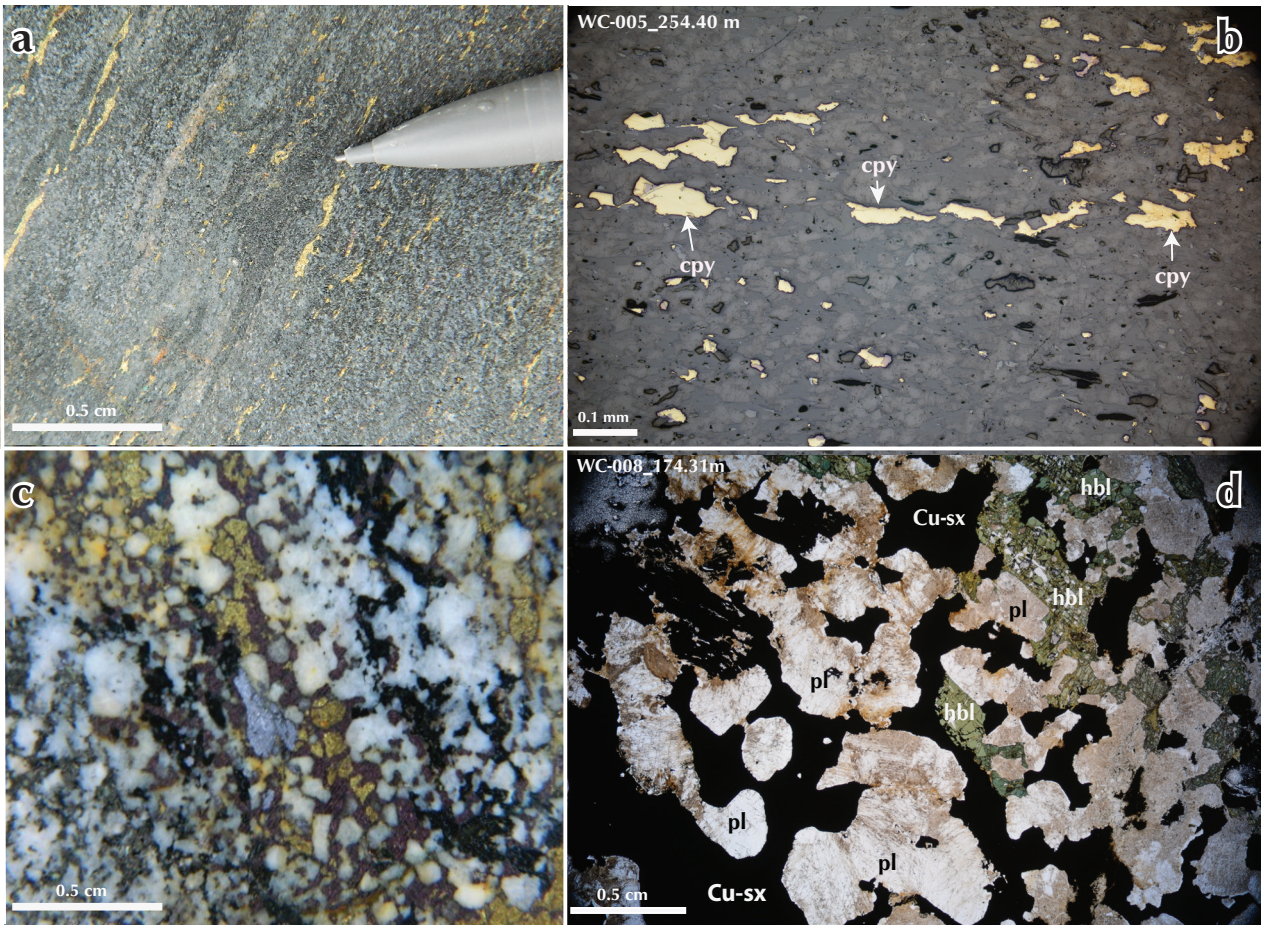

Figure 11. *Hypogene mineralization features:* ***(a)*** *foliation-parallel chalcopyrite stringers in feldspar-amphibole schist;* ***(b)*** *net-textured copper sulphides in migmatitic host rocks;* ***(c)*** *reflected light photomicrograph of foliation-parallel blebs and stringers of chalcopyrite in feldspar-amphibole schist; and* ***(d)*** *transmitted light photomicrograph of net-textured copper sulphides in migmatite host rocks (plane-polarized light). pl=plagioclase; hbl=hornblende; and Cu-sx=copper sulphide phase.*

DISCUSSION

The protolith(s) of the metamorphic rocks has been long debated at the Carmacks Copper deposit due to the complex overprinting history of metamorphism, deformation, and potentially, metasomatism.

However, variably foliated and mineralized, clinopyroxene-phyric metagabbro is locally present in gradational textural contact with mineralized plagioclase-amphibole schist. This association suggests that these rocks may represent the undeformed equivalent of this schist. The metagabbro is compositionally and texturally similar to augite-porphyritic basalt and coarse-grained, augite gabbro that are described from the Povoas formation of the Lewes River Group (Tempelman-Kluit, 1984). The closest known occurrence of Povoas formation is located 5 km from the Carmacks Copper deposit and is in intrusive contact with the Granite Mountain batholith. Mineralization in the Povoas formation is rare, but local small occurrences of chalcopyrite are known at Bonanza King (Yukon MINFILE 115I 010), Crossing (Yukon MINFILE 115I 077) and McCabe (Yukon MINFILE 115I 091) showings (Tempelman-Kluit, 1984). Further geochemical characterization of these rocks is required to draw comparisons; however, the potential presence of Povoas formation in the basement of the GMB may indicate affiliation with Stikinia rather than Yukon Tanana terrane.

Migmatite represents a new, coherent, mappable unit recognized on the Carmacks Copper deposit. Similar rocks were noted by Sinclair (1977) at the Minto deposit, who considered that foliated and mineralized zones of biotite granodiorite represent poorly digested, migmatized

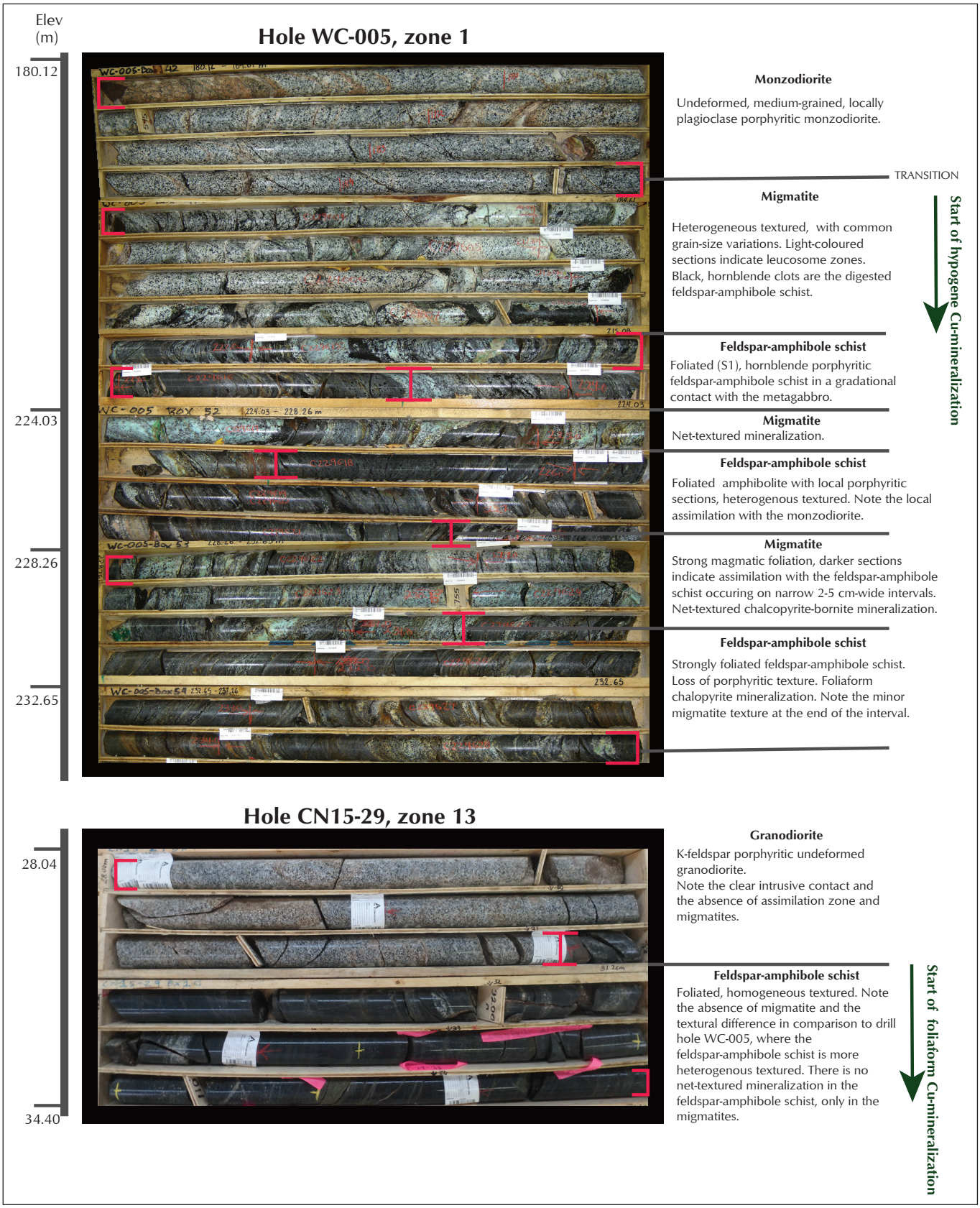

Figure 12. *Drill core sections representing the spatial relationship between monzodiorite of the eastern plutonic phase (I_1), migmatite, and schist from hole WC-005, zone 1.*

remnants of the Yukon Metamorphic Complex rocks (Yukon-Tanana terrane) that had either a sedimentary or volcanic protolith (Pearson and Clark, 1979; Sinclair, 1977). The common association of mineralization with migmatitic host rocks at both Carmacks Copper and Minto suggests that both deposits were affected by partial melting during emplacement of the Granite Mountain batholith.

Several ideas have been advanced to explain ore genesis in the Carmacks Copper belt. Based on our field and petrographic observations, the deposit model of the Carmacks Copper deposit must explain:

1. formation of foliation-parallel Cu-Au-Ag mineralization with negligible pyrite in mafic meta-igneous rocks, *i.e.*, ductile deformation of a previously mineralized mafic protolith at amphibolite facies;

2. formation of net-textured chalcopyrite-bornite rich ore in migmatitic rocks with virtually no hydrothermal alteration of silicate grains or replacement of mafic minerals by sulphides, *i.e.*, generation of a Cu-rich sulphide melt in the absence of a destabilizing hydrothermal fluid phase.

Because the Carmacks Copper deposit has been modified by ductile deformation, partial melting, and recycling of sulphide mineralization via a sulphide melt phase, a genetic model must initially account for mineralization of the protolith(s). In the case of Carmacks Copper, we infer that the main mineralized host rock was a mafic igneous rock (metagabbro?), and that Cu-Au-Ag mineralization was originally introduced from a metalliferous hydrothermal fluid.

CONCLUSION

Copper-gold-silver mineralization of the Carmacks Copper deposit was introduced early in the deposit's geologic evolution, presumably as hydrothermal mineralization of the mafic schist's igneous or sedimentary protolith(s). Ductile deformation and amphibolite facies metamorphism mobilized sulphide minerals into foliation-parallel blebs and stringers of sulphide. Metamorphic rocks were subsequently engulfed as inliers within the Late Triassic to Early Jurassic (Minto phase) Granite Mountain batholith. The eastern flank of the deposit is dominated by migmatite that presumably formed from the partial melting of metamorphic rocks during the intrusion of quartz-poor, alkaline monzodiorite to the east of the deposit. Pre-existing sulphides were recycled via a sulphide melt phase into net-textured copper sulphides in leucosome. The deposit was subsequently intruded to the west by subalkaline granodiorite. A second phase of compressional deformation preferentially affected rheologically incompetent metamorphic rocks, whereas plutonic rocks of the Granite Mountain batholith remained largely unstrained.

Ongoing investigations include U-Pb dating of various intrusive phases, Re-Os dating of molybdenite occurring in both foliaform and net-textured sulphide facies, Ar-Ar dating of hornblende and biotite to constrain cooling events, and 3D-modeling of the deposit to integrate surface mapping and drill core logging. Finally, lithogeochemical investigations of mineralized and unmineralized rocks at Carmacks Copper will reveal metasomatic trends of the protolith(s), which may elucidate the most likely ore deposit setting prior to deformation, metamorphism, and modification by magmatic processes.

ACKNOWLEDGEMENTS

The authors would like thank Copper North Mining Corp. for permission to publish this study and for logistical and financial support during the 2015–2016 field seasons. The Yukon Geological Survey is thanked for all of their in-kind support. Stephen Bartlett is thanked for being a great field assistant during the 2015-2016 field seasons. The authors are grateful to Maurice Colpron, Patrick Sack, Emily Halle, Scott Casselman, Jim Mortensen, John Chapman and Jesse Halle for stimulating discussions that have strengthened our field observations and interpretations. Kluane Drilling Ltd. is thanked for all their logistical support during camp set-up. This project is funded through a RAP bursary to Nikolett Kovacs from the Geological Survey Canada's Geo-Mapping for Energy and Minerals (GEM2) program, and through grants from Copper North Mining Corp. and NSERC CRD grant CRDPJ 488645-15. The manuscript benefitted from a critical review by Scott Casselman of the Yukon Geological Survey.

REFERENCES

Abbott, G., 1971. Geology of the Williams Creek copper prospect. Unpublished BASc. thesis, University of British Columbia, Canada, 22 p.

Allan, M.M., Mortensen, J., Hart, C., Bailey, L., Sánchez, M., Ciolkiewicz, W. and Creaser, R., 2013. Magmatic and metallogenic framework of west-central Yukon and eastern Alaska. Tectonics, Metallogeny, and Discovery: The North American Cordillera and Similar Accretionary Settings. Society of Economic Geologists Special Publication, vol. 17, p. 111-168.

Colpron, M., Crowley, J.L., Gehrels, G., Long, D.G.F., Murphy, D.C., Beranek, L. and Bickerton, L., 2015. Birth of the northern Cordilleran orogen, as recorded by detrital zircons in Jurassic synorogenic strata and regional exhumation in Yukon. Lithosphere, vol. 7, no. 5, p. 541-562.

Colpron, M., Sack, P.J., Crowley, J.L. and Allan, M.M., 2016a. Late Triassic to Middle Jurassic magmatism in the Intermontane terranes of Yukon. *In:* Geological Society of America Annual Meeting 2016, Abstract, <https://gsa.confex.com/gsa/2016AM/webprogram/Paper280151.html> [accessed November 27, 2016].

Colpron, M., Israel, S. and Friend, M. (comp.), 2016b. Yukon Plutonic Suites. Yukon Geological Survey, Open File 2016-37, scale 1:750 000.

Copper North Mining Corporation, 2016. Technical report (NI 43-101). System for Electronic Document Analysis and Retrieval (SEDAR), <http://www.sedar.com/FindCompanyDocuments.do> [accessed November 29, 2016].

Frost, B.R., Barnes, C.G., Collins, W.J., Arculus, R.J., Ellis, D.J. and Frost, C.D., 2001. A geochemical classification for granitic rocks. Journal of Petrology, vol. 42, p. 2033-2048.

Frost, B.R. and Frost, C.D., 2008. A geochemical classification for feldspathic igneous rocks. Journal of Petrology, vol. 49, p. 1955-1969.

Harris, N.B., Pearce, J.A. and Tindle, A.G., 1986. Geochemical characteristics of collision-zone magmatism. Geological Society, London, Special Publications, vol. 19, p. 67-81.

Hart, C.J.R., 1997. A transect across northern Stikinia: Geology of the northern Whitehorse map area, southern Yukon Territory (105D/13-16). *In:* Yukon Exploration and Geology 1997, J.K. Mortensen, M.J. Orchard, J. Palfy, H.W. Tipper and E.T. Tozer (eds.), Exploration and Geological Services Division, Yukon Region, Indian and Northern Affairs Canada, 112 p.

Hood, S., Hickey, K., Colpron, M. and Mercer, B., 2008. High-grade hydrothermal copper-gold mineralization in foliated granitoids at the Minto mine, central Yukon. *In*: Yukon Exploration and Geology 2008, L.H. Weston, L.R. Blackburn and L.L. Lewis (eds.), Yukon Geological Survey, p. 137-146.

Irvine, T. and Baragar, W., 1971. A guide to the chemical classification of the common volcanic rocks. Canadian Journal of Earth Sciences, vol. 8, no .5, p. 523-548.

Joyce, N.L., Colpron, M., Allan, M.M., Sack, P.J., Crowley, J.L and Chapman, J.B., 2016. New U-Pb zircon dates from the Aishihik batholith, southern Yukon. *In*: Yukon Exploration and Geology 2016, K.E. MacFarlane and M.G. Nordling (eds.), Yukon Geological Survey, p. 131-149.

Le Bas, M. and Streckeisen, A.L., 1991. The IUGS systematics of igneous rocks. Journal of the Geological Society, vol. 148, no. 5, p. 825-833.

Le Bas, M.J., Le Maitre, R., Streckeisen, A. and Zanettin, B., 1986. A chemical classification of volcanic rocks based on the total alkali-silica diagram. Journal of Petrology, vol. 27, no. 3, p. 745-750.

Nelson, J.L., Colpron, M. and Israel, S., 2013. The Cordillera of British Columbia, Yukon, and Alaska: Tectonics and metallogeny. *In:* Tectonics, Metallogeny and discovery: The North American Cordillera and similar accretionary setttings, M. Colpron, T. Bissig, B.G. Rusk and J.F. Thompson (eds.), Special Publication No. 17, Society of Economic Geologists, p. 53-109.

Pearce, J.A., 1996. A user's guide to basalt discrimination diagrams. *In:* Trace element geochemistry of volcanic rocks: applications for massive sulphide exploration, Wyman, D.A. (ed.), Geological Association of Canada, Short course notes, vol. 12, p. 79-113.

Pearce, J.A., Harris, N.B. and Tindle, A.G., 1984. Trace element discrimination diagrams for the tectonic interpretation of granitic rocks. Journal of Petrology, vol. 25, p. 956-983.

Pearson, W.N., 1977. The Minto copper deposit, Yukon Territory: a metamorphosed orebody in the Yukon Crystalline Terrane. Unpublished MSc thesis, Queen's University, Ontario, Canada, 195 p.

Pearson, W.N. and Clark, A.H., 1979. The Minto copper deposit, Yukon Territory; a metamorphosed orebody in the Yukon crystalline terrane. Economic Geology, vol. 74, p. 1577-1599

Sack, P.J., Casselman, S., James, D. and Harris, B., 2015. Copper-gold ± silver mineralization at the Stu occurrence, central Yukon (Yukon MINFILE 115I011). *In:* Yukon Exploration and Geology 2016, K.E. MacFarlane and M.G. Nordling (eds.), Yukon Geological Survey, p. 207-222, plus digital appendices.

Sánchez, M.G., Allan, M.M., Hart, C.J.R. and Mortensen, J.K., 2013. Orogen-perpendicular magnetic segmentation of the western Yukon and eastern Alaska cordilleran hinterland: Implications for structural control of mineralization. *In:* Yukon Exploration and Geology 2012, K.E. MacFarlane, M.G. Nordling and P.J. Sack (eds.), Yukon Geological Survey, p. 133-146.

Sinclair, W.D., 1977. Geology and mineral deposits of the Minto area, Yukon Territory. *In:* Mineral Industry Report, 1976, Exploration and Geological Services Division, Yukon Region, Indian and Northern Affairs Canada, EGS 1977-1, p. 68-80.

Tafti, R., 2005. Nature and origin of the early Jurassic copper (-gold) deposits at Minto and Williams Creek, Carmacks Copper Belt, Western Yukon: examples of deformed porphyry deposits. Unpublished MSc thesis, University of British Columbia, Canada, 212 p.

Tafti, R. and Mortensen, J.K., 2004. Early Jurassic porphyry (?) copper (-gold) deposits at Minto and Williams Creek, Carmacks copper belt, western Yukon. *In:* Yukon Exploration and Geology 2003, D.S. Edmond and L.L. Lewis (eds), Exploration and Geological Services Division, Yukon Region, Indian and Northern Affairs Canada, p. 289-303.

Tempelman-Kluit, D., 1984. Geology, Lebarge (105E) and Carmacks (115I) map areas, Yukon Territory. Geological Survey of Canada, Open File 1101.

Topham, M.J., Allan, M.M., Mortensen, J.K., Hart, C.J.R., Colpron, M. and Sack, P.J., 2016. Crustal depth of emplacement of the Early Jurassic Aishihik and Tatchun batholiths, west-central Yukon. *In:* Yukon Exploration and Geology 2015, K.E. MacFarlane and M.G. Nordling (eds.), Yukon Geological Survey, p. 233-251, including appendices.

Yukon Geological Survey, 2015. Yukon Digital Bedrock Geology. <http://www.geology.gov.yk.ca/update_yukon_bedrock_geology_map.html> [accessed November 7, 2016].

Yukon MINFILE, 2016. Yukon MINFILE – a database of mineral occurences. Yukon Geological Survey, <http://data.geology.gov.yk.ca > [accessed November 7, 2016].

Whalen, J.B., Currie, K.L. and Chappel, B.W., 1987. A-type granites: Geochemical characteristics, discrimination and petrogenesis. Contributions to Mineralogy and Petrology, vol. 95, p. 420-436.

Winchester, J. and Floyd, P., 1977. Geochemical discrimination of different magma series and their differentiation products using immobile elements. Chemical Geology, vol. 20, p. 325-343.

APPENDIX

Appendix 1. Whole-rock geochemical analyses. Whole-rock analysis of 20 samples was conducted at Bureau Veritas Commodities Canada Ltd., Vancouver, British Columbia, using the LF702-EXT and LF100-analytical packages, a lithium borate fusion followed by analysis using Inductively Coupled Plasma Mass Spectrometry (ICPMS). Major element oxides were analyzed by x-ray fluorescence (XRF) spectrometry. Samples were prepared using pulverization by ceramic box (100 g).

Using this analytical package, detection limits for major elements are 0.001% to 0.01% and trace elements are typically better than 1 ppm.

APPENDIX 1. *Whole-rock geochemical analyses.*

SampleID	Rock	SiO_2	Al_2O_3	Fe_2O_3	CaO	MgO	Na_2O	K_2O	MnO	TiO_2	P_2O_5
NK15-DS-002	Migmatite	63.39	19.07	2.71	3.47	1.12	5.92	1.55	0.05	0.32	0.28
NK15-DS-005	Diorite	59.63	21.42	3.57	4.84	1.21	6.89	1.33	0.07	0.42	0.19
NK15-026-Z4	Diorite	55.70	21.09	5.25	5.86	1.81	6.83	0.78	0.10	0.57	0.27
NK15-050-Z5	Diorite	57.94	21.38	2.70	4.16	1.30	7.73	1.02	0.04	0.26	0.15
NK15-085-Z13	Monzonite	62.90	16.59	5.15	4.09	1.98	4.70	3.05	0.12	0.49	0.29
NK15-074-Z12	Diorite	59.22	20.49	4.14	4.94	1.56	5.73	1.55	0.08	0.37	0.21
NK15-072-Z12	Gneiss	73.26	15.16	0.99	2.82	1.11	4.89	0.89	0.02	0.29	0.13
NK15-008-Z2	Diorite	42.49	17.37	13.63	4.88	5.60	2.90	2.04	0.15	1.43	0.80
NK15-079-Z2	Diorite	55.43	20.87	5.78	5.91	2.13	6.57	0.82	0.13	0.59	0.24
TR91-20-001	Diorite	56.71	20.98	5.27	6.09	1.94	6.79	1.01	0.10	0.59	0.27
TR91-20-006	Quartz Monzodiorite	64.57	20.25	1.53	3.52	0.60	7.18	1.05	0.03	0.19	0.06
TR91-20-012	Quartz Diorite	69.65	16.38	2.65	3.95	0.86	4.46	0.83	0.03	0.26	0.12
TR91-20-013	Monzonite	59.98	21.34	3.22	4.69	1.39	7.36	1.14	0.08	0.34	0.13
NK15-STU-001	Diorite	64.37	17.35	4.48	4.33	1.39	4.87	1.88	0.11	0.45	0.24
NK15-STU-002	Diorite	54.30	20.00	6.70	5.09	3.09	5.03	2.88	0.14	0.85	0.47
NK15-STU-004	Diorite	64.63	16.93	3.92	3.55	1.90	4.22	2.72	0.08	0.49	0.28
NK15-045-Z5	Granodiorite	65.99	17.05	3.50	4.02	1.16	5.08	1.82	0.08	0.35	0.16
WC-002-156.33	Monzodiorite	51.3	19.05	7.01	4.56	3.30	5.45	1.65	0.08	0.71	0.44
TR91-20-007	Quartz monzodiorite	67.7	17.99	1.47	2.55	0.56	5.81	2.06	0.03	0.19	0.07
TR91-20-005	Monzogranite	75.71	13.63	0.61	0.90	0.12	3.41	4.89	0.02	0.05	0.01

Appendix 1 continued

SampleID	Rock	Cr_2O_3	Ba	LOI	Ni	Pb	SO_3	Sr	V_2O_5	Zn	Zr
NK15-DS-002	Migmatite	<0.01	0.12	1.25	<0.001	<0.001	0.005	0.113	0.011	0.004	0.006
NK15-DS-005	Diorite	<0.01	0.13	0.69	<0.001	<0.001	0.004	0.155	0.016	0.006	0.007
NK15-026-Z4	Diorite	<0.01	0.07	0.83	<0.001	<0.001	<0.002	0.153	0.020	0.007	0.013
NK15-050-Z5	Diorite	<0.01	0.09	1.94	<0.001	<0.001	0.024	0.248	0.012	0.004	<0.002
NK15-085-Z13	Monzonite	<0.01	0.27	0.98	<0.001	0.002	<0.002	0.102	0.022	0.004	0.010
NK15-074-Z12	Diorite	<0.01	0.10	1.34	<0.001	<0.001	<0.002	0.106	0.018	0.006	0.011
NK15-072-Z12	Gneiss	<0.01	0.06	0.88	<0.001	<0.001	0.002	0.075	0.013	0.002	0.007
NK15-008-Z2	Diorite	<0.01	0.17	4.65	<0.001	<0.001	0.042	0.066	0.066	0.017	0.033
NK15-079-Z2	Diorite	<0.01	0.08	1.08	<0.001	<0.001	<0.002	0.138	0.021	0.008	0.015
TR91-20-001	Diorite	<0.01	0.10	0.62	<0.001	<0.001	0.003	0.160	0.021	0.006	0.015
TR91-20-006	Quartz Monzodiorite	<0.01	0.15	0.58	<0.001	<0.001	<0.002	0.170	0.007	0.002	<0.002
TR91-20-012	Quartz Diorite	<0.01	0.03	0.75	<0.001	<0.001	<0.002	0.058	0.012	0.002	0.007
TR91-20-013	Monzonite	<0.01	0.10	0.79	<0.001	<0.001	0.003	0.162	0.011	0.004	<0.002
NK15-STU-001	Diorite	<0.01	0.21	0.58	<0.001	<0.001	0.003	0.075	0.012	0.011	0.008
NK15-STU-002	Diorite	<0.01	0.18	1.18	<0.001	<0.001	0.010	0.091	0.030	0.012	0.014
NK15-STU-004	Diorite	<0.01	0.17	0.71	<0.001	<0.001	0.006	0.084	0.020	0.007	0.007
NK15-045-Z5	Granodiorite	<0.01	0.23	0.81	<0.001	<0.001	<0.002	0.102	0.013	0.005	0.006
WC-002-156.33	Monzodiorite	0.002	0.14	2.70	<0.01	<0.01	0.094	0.130	0.030	0.013	0.016
TR91-20-007	Quartz monzodiorite	<0.001	0.38	0.92	<0.01	<0.01	<0.002	0.126	0.005	0.003	0.005
TR91-20-005	Monzogranite	<0.01	0.61	0.34	<0.001	0.004	<0.002	0.066	0.003	<0.001	<0.002

Appendix 1 continued

SampleID	Rock	SUM	TOT/C	TOT/S	Ba	Be	Co	Cs	Ga	Hf	Nb
NK15-DS-002	Migmatite	100.18	<0.02	<0.02	1173	<1	4.9	0.3	19.5	3.0	1.8
NK15-DS-005	Diorite	100.84	<0.02	<0.02	1411	<1	5.8	0.2	22.6	3.1	2.9
NK15-026-Z4	Diorite	99.41	<0.02	<0.02	746	<1	8.0	<0.1	22.6	3.4	3.7
NK15-050-Z5	Diorite	99.20	0.20	<0.02	1091	1	6.9	0.3	20.7	1.6	0.9
NK15-085-Z13	Monzonite	100.79	<0.02	<0.02	2879	1	7.7	0.3	17.3	3.2	11.0
NK15-074-Z12	Diorite	100.28	<0.02	<0.02	1013	4	11.2	0.8	21.1	3.7	4.5
NK15-072-Z12	Gneiss	100.73	0.02	<0.02	619	<1	2.5	0.4	18.5	3.0	6.2
NK15-008-Z2	Diorite	99.73	0.03	0.07	1666	2	51.4	1.7	27.8	9.1	14.4
NK15-079-Z2	Diorite	99.85	<0.02	<0.02	816	2	10.7	0.2	23.8	3.8	4.0
TR91-20-001	Diorite	100.72	<0.02	<0.02	1062	<1	7.8	<0.1	22.6	3.8	3.2
TR91-20-006	Quartz Monzodiorite	99.94	<0.02	<0.02	1569	<1	3.1	0.2	16.0	1.0	0.6
TR91-20-012	Quartz Diorite	100.08	<0.02	<0.02	291	2	3.4	1.4	18.9	2.7	3.1
TR91-20-013	Monzonite	100.77	0.03	<0.02	1058	2	6.5	0.1	21.0	1.4	3.4
NK15-STU-001	Diorite	100.40	<0.02	<0.02	2207	3	6.0	0.4	18.1	3.6	5.5
NK15-STU-002	Diorite	100.57	<0.02	<0.02	1866	3	14.5	1.2	23.5	5.4	10.3
NK15-STU-004	Diorite	100.13	0.02	<0.02	1786	<1	8.9	0.8	17.2	2.9	6.4
NK15-045-Z5	Granodiorite	100.41	<0.02	<0.02	2344	2	5.8	0.1	21.0	3.3	6.6
WC-002-156.33	Monzodiorite	100.15	0.03	0.81	1386	<1	14.3	0.5	26.3	6.1	5.9
TR91-20-007	Quartz monzodiorite	99.99	0.02	<0.02	3915	<1	3.7	0.6	14.5	1.6	2.0
TR91-20-005	Monzogranite	100.49	<0.02	<0.02	6508	<1	0.8	0.3	10.2	0.5	0.2

Appendix 1 continued

SampleID	Rock	Rb	Sn	Sr	Ta	Th	U	V	W	Zr	Y	La	Ce
NK15-DS-002	Migmatite	45.0	2	1200.0	<0.1	6.6	0.8	55	3.6	116.4	6.0	19.5	34.7
NK15-DS-005	Diorite	24.2	<1	1716.4	0.2	0.6	0.4	68	<0.5	134.3	8.5	6.0	13.1
NK15-026-Z4	Diorite	6.3	1	1620.8	0.2	1.8	0.3	92	<0.5	149.5	13.2	17.0	34.5
NK15-050-Z5	Diorite	16.7	<1	2553.0	<0.1	0.4	0.3	58	1.0	49.0	5.7	3.5	7.4
NK15-085-Z13	Monzonite	52.4	2	1032.4	0.7	7.1	2.6	98	0.5	114.2	20.7	21.8	45.6
NK15-074-Z12	Diorite	52.9	1	1156.2	0.2	2.7	0.4	76	0.8	141.1	15.4	19.3	34.7
NK15-072-Z12	Gneiss	19.4	3	767.7	0.4	12.7	1.4	57	<0.5	93.9	11.0	6.1	14.2
NK15-008-Z2	Diorite	96.9	3	756.3	0.7	25.1	4.4	332	0.7	336.5	28.5	44.3	81.4
NK15-079-Z2	Diorite	11.7	2	1594.0	0.2	1.1	0.4	104	<0.5	153.5	13.0	10.0	21.9
TR91-20-001	Diorite	10.1	2	1795.9	<0.1	1.4	0.3	89	<0.5	152.5	14.0	14.3	33.2
TR91-20-006	Quartz Monzodiorite	17.3	<1	1813.5	<0.1	0.4	<0.1	20	0.6	41.1	0.9	3.1	4.7
TR91-20-012	Quartz Diorite	44.2	<1	706.7	0.2	5.1	0.8	48	0.9	104.2	4.3	8.6	16.7
TR91-20-013	Monzonite	18.9	<1	1797.8	<0.1	0.3	0.2	55	<0.5	52.4	7.9	3.1	8.3
NK15-STU-001	Diorite	35.4	1	908.9	0.3	2.3	0.5	55	<0.5	135.3	16.3	16.3	34.1
NK15-STU-002	Diorite	102.2	2	1125.5	0.4	2.8	1.9	145	<0.5	208.1	18.9	19.7	38.6
NK15-STU-004	Diorite	89.1	<1	882.6	0.2	8.2	1.0	98	<0.5	105.9	8.2	24.7	44.3
NK15-045-Z5	Granodiorite	24.5	<1	1217.4	0.4	1.9	0.6	69	<0.5	126.6	12.0	15.4	30.6
WC-002-156.33	Monzodiorite	44.8	2	1441.6	0.3	2.7	1.2	171	0.8	233.3	16.4	14.9	31.1
TR91-20-007	Quartz monzodiorite	40.9	<1	1281.8	<0.1	<0.2	<0.1	37	0.6	53.6	1.2	2.5	5.5
TR91-20-005	Monzogranite	59.3	<1	765.0	<0.1	<0.2	0.2	<8	1.0	20.4	1.0	0.8	1.4

Appendix 1 continued

SampleID	Rock	Pr	Nd	Sm	Eu	Gd	Tb	Dy	Ho	Er	Tm	Yb
NK15-DS-002	Migmatite	3.36	12.1	1.88	0.46	1.45	0.17	0.94	0.20	0.48	0.08	0.55
NK15-DS-005	Diorite	1.93	8.2	1.59	0.55	1.79	0.25	1.54	0.29	0.90	0.13	0.91
NK15-026-Z4	Diorite	4.08	17.1	3.11	0.88	3.08	0.39	2.66	0.43	1.24	0.20	1.25
NK15-050-Z5	Diorite	1.12	5.4	1.14	0.39	1.35	0.16	0.99	0.21	0.52	0.08	0.46
NK15-085-Z13	Monzonite	5.34	24.3	4.35	0.85	4.15	0.53	3.47	0.72	2.23	0.29	2.31
NK15-074-Z12	Diorite	4.11	14.7	2.51	0.75	2.69	0.36	2.37	0.47	1.47	0.18	1.35
NK15-072-Z12	Gneiss	2.01	8.9	2.11	0.43	2.17	0.31	2.08	0.40	1.15	0.16	1.20
NK15-008-Z2	Diorite	9.27	36.2	7.05	1.42	6.63	0.84	5.33	0.94	2.58	0.42	2.60
NK15-079-Z2	Diorite	2.71	11.6	2.40	0.77	2.70	0.33	2.11	0.46	1.34	0.18	1.17
TR91-20-001	Diorite	3.99	16.6	3.61	0.97	3.21	0.44	2.79	0.50	1.38	0.21	1.29
TR91-20-006	Quartz Monzodiorite	0.49	1.7	0.14	0.08	0.16	0.02	0.15	0.03	0.09	0.01	0.14
TR91-20-012	Quartz Diorite	1.20	3.7	0.56	0.34	0.74	0.09	0.64	0.14	0.53	0.07	0.57
TR91-20-013	Monzonite	1.42	6.9	1.86	0.59	1.89	0.24	1.75	0.33	0.88	0.12	0.80
NK15-STU-001	Diorite	4.27	17.4	4.28	0.95	4.55	0.54	3.42	0.57	1.70	0.25	1.69
NK15-STU-002	Diorite	5.18	21.1	4.25	1.09	4.17	0.59	3.55	0.65	2.02	0.29	1.98
NK15-STU-004	Diorite	4.87	17.8	2.96	0.51	2.55	0.30	1.80	0.26	0.76	0.11	0.71
NK15-045-Z5	Granodiorite	3.76	14.8	3.15	0.77	2.66	0.40	2.18	0.45	1.48	0.19	1.35
WC-002-156.33	Monzodiorite	3.96	15.7	3.28	0.92	3.55	0.49	2.82	0.55	1.68	0.22	1.64
TR91-20-007	Quartz monzodiorite	0.45	2.1	0.14	0.13	0.36	0.04	0.29	0.06	0.18	0.02	0.20
TR91-20-005	Monzogranite	0.13	0.6	<0.05	<0.02	0.21	0.01	0.07	0.02	0.07	0.02	0.14

Appendix 1 continued

SampleID	Rock	Lu	Cd	Sb	Bi	Hg	Tl	Se
NK15-DS-002	Migmatite	0.09	0.2	<0.1	0.1	<0.01	0.1	<0.5
NK15-DS-005	Diorite	0.12	0.2	<0.1	<0.1	0.01	<0.1	<0.5
NK15-026-Z4	Diorite	0.23	<0.1	<0.1	<0.1	<0.01	<0.1	<0.5
NK15-050-Z5	Diorite	0.08	0.2	<0.1	0.6	<0.01	<0.1	<0.5
NK15-085-Z13	Monzonite	0.34	<0.1	<0.1	<0.1	<0.01	<0.1	<0.5
NK15-074-Z12	Diorite	0.22	0.2	<0.1	<0.1	<0.01	0.1	<0.5
NK15-072-Z12	Gneiss	0.15	<0.1	<0.1	0.4	0.01	<0.1	<0.5
NK15-008-Z2	Diorite	0.43	1.9	<0.1	30.3	0.26	0.3	3.7
NK15-079-Z2	Diorite	0.17	<0.1	<0.1	<0.1	<0.01	<0.1	<0.5
TR91-20-001	Diorite	0.18	<0.1	<0.1	<0.1	<0.01	<0.1	<0.5
TR91-20-006	Quartz Monzodiorite	0.02	<0.1	<0.1	<0.1	<0.01	<0.1	<0.5
TR91-20-012	Quartz Diorite	0.10	<0.1	<0.1	<0.1	<0.01	0.2	<0.5
TR91-20-013	Monzonite	0.12	<0.1	<0.1	<0.1	<0.01	<0.1	<0.5
NK15-STU-001	Diorite	0.26	<0.1	<0.1	<0.1	<0.01	0.1	<0.5
NK15-STU-002	Diorite	0.32	0.1	<0.1	1.7	0.01	0.4	0.6
NK15-STU-004	Diorite	0.12	0.3	<0.1	2.0	<0.01	0.4	<0.5
NK15-045-Z5	Granodiorite	0.22	<0.1	<0.1	<0.1	<0.01	<0.1	<0.5
WC-002-156.33	Monzodiorite	0.23	0.6	<0.1	25.7	0.02	<0.1	4.9
TR91-20-007	Quartz monzodiorite	0.04	<0.1	<0.1	<0.1	<0.01	<0.1	<0.5
TR91-20-005	Monzogranite	0.03	<0.1	<0.1	<0.1	<0.01	<0.1	<0.5